Ligand-Based Redox Isomers of $[Zn^{II}(C_{28}H_{40}NO_2)_2]$: Molecular and Electronic Structures of a Diamagnetic Green and a Paramagnetic Red Form

Phalguni Chaudhuri,* Martina Hess, Knut Hildenbrand, Eckhard Bill, Thomas Weyhermüller, and Karl Wieghardt*

Max-Planck-Institut für Strahlenchemie, Stiftstrasse 34-36, D-45470 Mülheim an der Ruhr, Germany

Received January 6, 1999

The tridentate trianion of *N*,*N*-bis(2-hydroxy-di-3,5-*tert*-butylphenyl)amine, H_3L^3, forms 1:1 and 2:2 complexes with di-, tri-, or tetravalent transition metal ions where it can exist in four oxidation levels $(C_{28}H_{40}NO_2)^{3-,2-,1-,0}$, which are herein designated as L^3, L^2, L^1, and L^0, respectively; $(L^2)^{2-}$ and $(L^0)^0$ are paramagnetic ($S = {}^1/_2$), whereas the other two are diamagnetic ($S = 0$). We have synthesized the complexes $[Zn(L^2)(NEt_3)]$ (**1**), green $[Zn(L^1)_2]$ (**2**), and red $[Zn(L^2)(L^0)]$ (**3**). Complexes **1**, **2** (Girgis, A. Y.; Balch, A. L. *Inorg. Chem.* **1975**, *14*, 2724), and **3** have been characterized by X-ray crystallography: **1**, orthorhombic, *Iba*2, $a = 23.194(4)$ Å, $b = 25.132(4)$ Å, $c = 11.741(2)$ Å, $V = 6844(2)$ Å^3, $Z = 8$; **2**, orthorhombic, $C222_1$, $a = 19.494(3)$ Å, $b = 24.065(4)$ Å, $c = 23.458(4)$ Å, $V = 11004(3)$ Å^3, $Z = 8$; **3**, triclinic, $P\bar{1}$, $a = 11.677(2)$ Å, $b = 12.192(2)$ Å, $c = 20.522(3)$ Å, $\alpha = 83.68(2)$, $\beta = 74.37(2)$, $\gamma = 75.40(2)^o$, $V = 2720.0(8)$ Å^3, $Z = 2$. Complexes **1** and **3** are paramagnetic with one and two (uncoupled) unpaired electrons per zinc ion (3−290 K), respectively, whereas **2** is diamagnetic. Complexes **2** and **3** are shown to be ligand-based redox isomers. Red **3** converts into the green form **2** in tetrahydrofuran solution under anaerobic conditions via an intramolecular process ($k = 0.7 \times 10^{-3}$ s^{-1} at 23 °C; $\Delta H^{\ddagger} = 15.6 \pm 0.6$ kcal mol^{-1}, $\Delta S^{\ddagger} = -20.4 \pm 1.8$ cal mol^{-1} K^{-1}). The electronic structures of **1** and **3** have been investigated by X-band EPR and ^{1}H NMR spectroscopy. The electro-, spectroelectrochemistry, and magnetochemistry of all complexes are reported.

Introduction

The coordination chemistry of the tridentate trianion of *N*,*N*-bis(2-hydroxy-di-3,5-*tert*-butylphenyl)amine, H_3L^3, has attracted considerable scientific interest[1−8] since Girgis and Balch's original paper in 1975.[2] This is mainly due to the fact that this coordinated anion displays a rich and diverse redox chemistry. Four oxidation levels of the $(C_{28}H_{40}NO_2)^{n-}$ anions have been identified that are interrelated by one-electron-transfer steps ($n = 3, 2, 1, 0$). Scheme 1 shows one of many possible resonance structures for each of these ligands. Here we adopt[6] a labeling scheme for these ligands as L^n, where the superscript *n* indicates the anionic charge of the respective ligand. Previous authors[1−8] have chosen somewhat longer acronyms where the oxidataion level of the N-bound phenolate rings is highlighted, e.g., $(L^3)^{3-} = (Cat\text{-}N\text{-}Cat)^{3-}$, $(L^2)^{2-} = (Cat\text{-}N\text{-}SQ)^{2-}$, $(L^1)^{1-} = (Cat\text{-}N\text{-}BQ)^{1-}$, and $L^0 = (BQ\text{-}N\text{-}SQ)^0$; SQ represents the iminosemiquinone level, BQ is the corresponding iminobenzoquinone, and Cat is the catecholate. Note that L^2 and L^0 are paramagnetic ligands with an $S_L = {}^1/_2$ ground state, whereas L^3 and L^1 are diamagnetic ($S_L = 0$).

A number of complexes of the type $[M(L^n)_2]$ have been synthesized and characterized by X-ray crystallography; they are assembled in Table 1. All of the species in Table 1 are neutral molecules, containing two meridionally coordinated tridentate $(C_{28}H_{40}NO_2)^{n-}$ ligands. If the central metal ion is divalent (and redox-inactive) as in the case of Pb^{II}, Mg^{II}, Zn^{II}, and Cd^{II}, then each of the two ligands has been assigned a uninegative charge $(L^1)^-$. Consequently, these complexes are diamagnetic. Thus, Balch's green zinc complex[2] is formulated as $[Zn^{II}(L^1)_2]$ species. We report, herein, its crystal structure, which serves as a structural benchmark for coordinated $(L^1)^-$. The structure of $[Zn(L^1)_2]$ has been briefly mentioned in refs 7 and 9 without giving full details; it crystallizes in the orthorhombic space group $C222_1$.

If the central metal ion is trivalent as in the cobalt(III)[3] and iron(III)[4] species, then the two ligands cannot have the same oxidation level; the magnetism and EPR spectra support a charge distribution as $[M^{III}(L^2)(L^1)]$. This difference is not borne out by their crystal structures where the C−C, C−O, and C−N distances of the two different ligands are very similar. In cases

(1) Pierpont, C. G.; Lange, C. W. *Prog. Inorg. Chem.* **1994**, *41*, 331.
(2) Girgis, A. Y.; Balch, A. L. *Inorg. Chem.* **1975**, *14*, 2724.
(3) Larsen, S. K.; Pierpont, C. G. *J. Am. Chem. Soc.* **1988**, *110*, 1827.
(4) Simpson, C. L.; Boone, S. R.; Pierpont, C. G. *Inorg. Chem.* **1989**, *28*, 4379.
(5) Caneschi, A.; Dei, A.; Gatteschi, D. *J. Chem. Soc., Chem. Commun.* **1992**, 630.
(6) Bruni, S.; Caneschi, A.; Cariati, F.; Delfs, C.; Dei, A.; Gatteschi, D. *J. Am. Chem. Soc.* **1994**, *116*, 1388.
(7) Speier, G.; Csihony, J.; Whalen, A. M.; Pierpont, C. G. *Inorg. Chem.* **1996**, *35*, 3519.
(8) (a) McGarvey, B. R.; Ozarowski, A.; Tian, Z.; Tuck, D. G. *Can. J. Chem.* **1995**, *73*, 1213. (b) Bencini, A.; Ciofini, I.; Giannasi, E.; Daul, C. A.; Doclo, K. *Inorg. Chem.* **1998**, *37*, 3719. (b) Jung, O.-S.; Jo, D. H.; Lee, Y. A.; Sohn, Y. S.; Pierpont, C. G. *Inorg. Chem.* **1998**, *37*, 5875.
(9) Scotto, C. S. Ph.D. Thesis, University of Colorado, Boulder, 1992.

10.1021/ic990003g CCC: $18.00
Published on Web 05/21/1999

Scheme 1

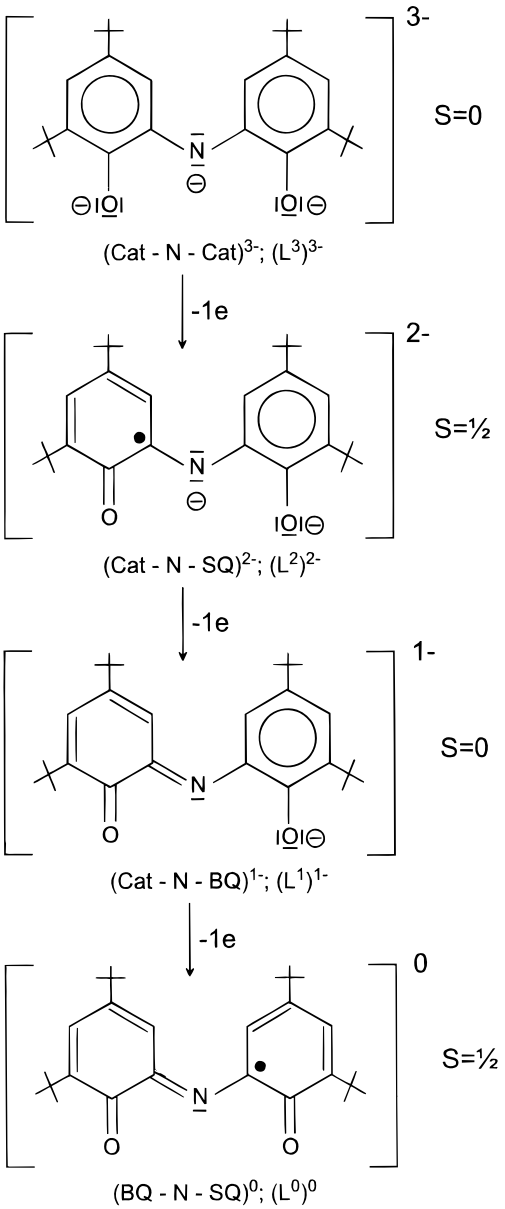

Table 1. List of Structurally Characterized Complexes $[M(L^n)_2]$

complex	space group	dihedral angles, deg[a]	S_t[b]	ref
$[M^{II}(L^1)_2]$				
Mg, Cd	n.d.	n.d.	0	2
Pb	$P2_1/n$		0	8a
Zn (green)	$C222_1$	29.2; 31.3	0	7, *b*
$[Zn(L^2)(L^0)]$ (red)	$P\bar{1}$	13.6; 8.9	$S_{L0} = {}^1/_2$; $S_{L2} = {}^1/_2$	*b*
Ni	$P\bar{1}$	12.6; 4.9	1	4
Cu	$C222_1$	33.8; 27.6	${}^1/_2$	7
$[M^{II}(L^1)(L^2)]$				
Fe	$P\bar{1}$	11.7; 4.9	2	4
Co	$P\bar{1}$	13.1; 0.7	${}^1/_2$	3
$[M^{IV}(L^2)_2]$				
Ti	$P\bar{1}$	10.0; 5.4	1	5, 6
V	$P\bar{1}$	9.7; 5.3	${}^1/_2$	6
Mn	$P\bar{1}$	13.4; "planar"	${}^1/_2$	3
Sn	$C222_1$	30.4; 28.7	1	8a, 8b
Ge	n.d.	n.d.	1	6

[a] Dihedral angle between the two planes defined by the two six-membered carbon rings of each ligand L^n. [b] Ground state of the molecule $[M(L^n)_2]$. n.d. = not determined. [b] This work.

where the central metal ion has a partially filled t_{2g} subshell,e.g., high-spin Fe^{III}, strong intramolecular antiferromagnetic coupling between the metal d electrons and the unpaired electron of $(L^2)^{2-}$ prevails, yielding an $S_t = 2$ ground state for the iron(III) complex.

Finally, all $[M^{IV}(L^2)_2]$ complexes[5,6] have been shown to contain two paramagnetic $(L^2)^{2-}$ ligands, which in the cases of Ti^{IV}, Sn^{IV}, and Ge^{IV} yields via an intramolecular ferromagnetic interaction a triplet ground state ($S_t = 1$). In contrast, for the $V^{IV}(d^1)$ and $Mn^{IV}(d^3)$ species, intramolecular antiferromagnetic coupling between the d^n electrons and two ligand radical spins yields an $S_t = {}^1/_2$ ground state, respectively.

In this paper, we report the synthesis and crystal structures of the known diamagnetic green form of $[Zn(L^1)_2]$ and of its isomeric red and paramagnetic form $[Zn(L^2)(L^0)]$. The latter represents a ligand-based redox isomer of Balch's complex and is the first example where the oxidation levels of the two coordinated L^n ligands in a complex differ formally by *two* electrons.

Experimental Section

A convenient, simple synthesis of *N*,*N*-bis(2-hydroxy-3,5-di-*tert*-butylphenyl)ammonium trifluoracetate, $[H_4L^3](CF_3CO_2)$, has been described recently.[10]

$[Zn^{II}(L^2)(NEt_3)]$ (1). A solution of $[H_4L^3](CF_3CO_2)$ (0.54 g; 1.0 mmol), $Zn(acetate)_2\ 2H_2O$ (0.22 g; 1.0 mmol), and triethylamine (0.5 mL) in freshly distilled, dry methanol (50 mL) was heated to reflux under an argon atmosphere for 30 min. The yellow solution was then exposed to air and stirred at 20 °C for 20 min whereupon a color change to deep green was observed. Addition of tetra-*n*-butylammonium perchlorate (0.34 g) initiated the precipitation of dark green crystals of **1** (salt effect). Yield: 360 mg (61%). Anal. Calcd for green $C_{34}H_{55}N_2O_2Zn$: C, 69.31; H, 9.41; N, 4.75; Zn, 11.09. Found: C, 69.5; H, 9.2; N, 4.6; Zn, 10.7.

$[Zn^{II}(L^1)_2]$, Green (2). This complex has been originally reported by Balch et al.[2] We have used a slightly different protocol. A solution of $[H_4L^3](CF_3CO_2)$ (1.08 g; 2.0 mmol), $Zn(ClO_4)_2{\cdot}6H_2O$ (0.37 g; 1.0 mmol), and NEt_3 (0.5 mL) in freshly distilled, dry methanol was heated to reflux under an argon blanketing atmosphere for 30 min. The cooled yellow solution (20 °C) was then stirred in the presence of air until a dark green microcrystalline precipitate had formed. Yield: 510 mg (56%). Anal. Calcd for $C_{56}H_{80}N_2O_4Zn$: C, 73.87; H, 8.86; N, 3.08; Zn, 7.18. Found: C, 73.5; H, 8.6; N, 3.0; Zn, 7.1.

$[Zn^{II}(L^0)(L^2)]$, Red (3). A solution of $[H_4L^3](CF_3CO_2)$ (540 mg; 1.0 mmol), $Zn(BF_4)_2{\cdot}XH_2O$ (240 mg; 1.0 mmol), and NEt_3 (0.2 mL) in freshly distilled, dry acetonitrile was heated to reflux under an argon blanketing atmosphere for 30 min. The cooled (20 °C) colorless solution was exposed to air with stirring whereupon the color changed to green within ~2 min. Upon addition of *n*-pentane (10 mL), a dark green precipitate of **2** formed within 5−10 min, which was filtered off. Yield: 80 mg. To the resulting red-violet solution was added tetra-*n*-butylammonium perchlorate (360 mg). When the solution was allowed to stand at ambient temperature for 12 h, red crystals of **3** formed. Yield: 30 mg. If CH_3OH is used as solvent under otherwise the same conditions as above, the only isolable product is green **2**. Larger amounts of NEt_3 in the above synthesis produce also only **2**. When the ligand/Zn ratio is changed from 1:1 to 2:1, the formation of **2** (90%) is favored again and gave only ~10% of red **3**. Anal. Calcd for red $C_{56}H_{80}N_2O_4Zn$: C, 73.87; H, 8.86; N, 3.08; Zn, 7.18. Found: C, 73.6; H, 8.6; N, 3.0; Zn, 7.1.

Physical Measurements. Electronic spectra of the complexes and spectra of the spectroelectrochemical investigations were recorded on a Perkin-Elmer Lambda 19 (range: 220−1400 nm) and on a HP 8452A diode array spectrophotometer (range: 220−820 nm), respectively. Cyclic voltammograms, square-wave voltammograms, and coulometric

(10) Chaudhuri, P.; Hess, M.; Weyhermüller, T.; Wieghardt, K. *Angew. Chem.*, **1999**, *111*, *1165*. *Angew. Chem., Int. Ed. Engl.* **1999**, *38*, 1095.

Table 2. Crystallographic Data for **1**, **2**, and **3**

	1	**2**	**3**
chem formula	$C_{34}H_{55}N_2O_2Zn$	$C_{56}H_{80}N_2O_4Zn$	$C_{56}H_{80}N_2O_4Zn$
fw	589.17	910.59	910.59
space group	*I*ba2	$C222_1$	$P\bar{1}$
a, Å	23.194(4)	19.494(3)	11.677(2)
b, Å	25.132(4)	24.065(4)	12.192(2)
c, Å	11.741(2)	23.458(4)	20.522(3)
α, deg	90	90	83.68(2)
β, deg	90	90	74.37(2)
γ, deg	90	90	75.40(2)
V, Å	6844(2)	11004(3)	2720.0(8)
Z	8	8	2
T, K	100(2)	100(2)	100(2)
ρ calcd, g cm^{-3}	1.144	1.099	1.112
μ(Mo Kα), cm^{-1}	7.47	4.89	4.94
refl. collected	30196	39707	23051
unique refl./[$I > 2\sigma(I)$]	7345/6504	7747/7119	10270/6575
no. of parameters	367	577	592
$2\theta_{max}$, deg	55.0	48.8	52.0
R1[a] [$I > 2\sigma(I)$]	0.0407	0.0356	0.0551
wR2[b] [$I > 2\sigma(I)$]	0.0948	0.0808	0.1061

[a] $R1 = \sum||F_o| - |F_c||/\sum|F_o|$. [b] $wR2 = [\sum[w(F_o^2 - F_c^2)^2]/\sum[w(F_o^2)^2]]^{1/2}$ where $w = 1/\sigma^2(F_o^2) + (aP)^2 + bP$, $P = (F_o^2 + 2F_c^2)/3$.

experiments were performed on EG&G equipment (potentiostat/galvanostat model 273 A). EPR spectra of complexes were measured at 298 K in a quartz cell ($d = 0.3$ mm). The data were digitized on a data station (Stelar snc, Mede, Italy). The spectra were simulated by iteration of the isotropic hyperfine coupling constants and line widths, a and $\Delta\nu_{1/2}$. We thank Dr. F. Neese (Abteilung Biologie der Universität Konstanz) for a copy of his EPR simulation program. Temperature-dependent (2−298 K) magnetiztion data were recorded on a SQUID magnetometer (MPMS Quantum Design) in an external magnetic field of 1.0 T. The experimental susceptibility data were corrected for underlying diamagnetism by use of tabulated Pascal's constants. The kinetics of the conversion **3** → **2** was measured spectrophotometrically by following the decrease of absorbance (A) at 548 nm of **3** in freshly distilled dry tetrahydrofuran as a function of time and temperature. The data were readily fitted to a single-exponential expression $A(t) = \Delta A \exp(-kt) + A_o$. From the temperature dependence of k_{obs}, values for $\Delta H^{\ddagger}$ and $\Delta S^{\ddagger}$ were determined by a least-squares fit of the data to the Eyring equation.

X-ray Crystallographic Data Collection and Refinement of the Structures. Green single crystals of **1** and **2** and a red crystal of **3** were transferred to glass capillaries and sealed under argon. Samples **1** and **3** were mounted on a Siemens SMART CCD-detector diffractometer, whereas **2** was measured on a Nonius Kappa-CCD diffractometer. Both setups were equipped with a cryogenic nitrogen cold stream. Graphite monochromated Mo Kα radiation ($\lambda = 0.710\ 73$ Å) was used throughout. Crystallographic data of the compounds are listed in Table 2. Cell constants were obtained from a least-squares fit of a subset of at least 4430 strong reflections. Intensity data were collected at −173(2) °C by a hemisphere run taking frames at 0.30° in ω. Data were corrected for Lorentz and polarization effects, and **1** and **3** were also corrected for absorption, using the program SADABS (G. M. Sheldrick, University Göttingen 1994). Equivalent reflections were merged but Friedel opposites of **1** and **2** were left unchanged in order to determine the absolute structure of these compounds, crystallizing in noncentrosymmetric space groups. The Siemens ShelXTL[11a] software package was used for solution, refinement, and artwork of the structures. All structures were solved and refined by direct methods and difference Fourier techniques. Neutral atom scattering factors were obtained from tables.[11b] All non-hydrogen atoms were refined anisotropically. Hydrogen atoms were placed at calculated positions and refined as riding atoms with isotropic displacement parameters. A tertiary butyl group was found to be disordered in **2** (C40, C41, C42). The disorder was modeled by a split atom model with occupancies of 0.5 for each of the six resulting carbon positions.

(11) (a) ShelXTL V.5, Siemens Analytical X-ray Instruments, Inc. 1994. (b) *International Tables for X-ray Crystallography*; Kynoch Press: Birmingham, U.K., 1991.

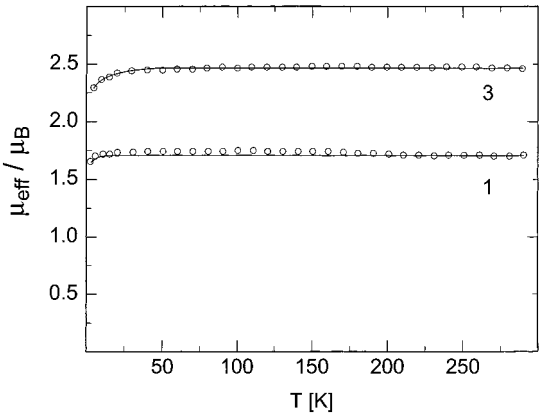

Figure 1. Temperature dependence of the magnetic moment per zinc ion, μ_{eff}, of **1** and **3**. The solid line for **3** represents a fit using the Hamiltonian $H = -2\mathbf{J}\mathbf{S}_1\cdot\mathbf{S}_2$. For parameters, see text.

Results and Discussion

Synthesis and Characterization of Complexes. Girgis and Balch[2] have reported the synthesis of diamagnetic green $[Zn(L^1)_2]$ (**2**) in 80% yield via a condensation reaction of 3,5-di-*tert*-butylcatechol and NH_3 in the presence of oxygen and Zn(acetate)$_2$·2H$_2$O in ethanol. Thus, the tridentate ligand $(L^1)^-$ was prepared in situ under oxidative conditions. These authors also mentioned an alternative route by co-condensation of 3,5-di-*tert*-butyl-1,2-benzoquinone, 3,5-di-*tert*-butylcatechol, NH_3, and zinc acetate under anaerobic conditions.

We have recently reported the synthesis of colorless *N*,*N*-bis(3,5-di-*tert*-butyl-2-hydroxyphenyl)ammonium trifluoracetate, $[H_4L^3](CF_3CO_2)$,[10] which reacts with metal ions under anaerobic or aerobic conditions, yielding a variety of mono- and bis-(chelate)metal complexes. Thus, the reaction of $[H_4L^3](CF_3CO_2)$, Zn(acetate)$_2$·2H$_2$O (1:1), and NEt_3 in dry methanol under anaerobic conditions yields a pale yellow solution from which upon exposure to air dark green crystals of $[Zn^{II}(L^2)(NEt_3)]$ (**1**) precipitated in ∼60% yield. Complex **1** is paramagnetic with a temperature independent magnetic moment of 1.73(1) μ_B (10−290 K) and $g = 2.002$ (Figure 1).

With a change of the ligand/zinc ratio to 2:1 and with otherwise identical reaction conditions, dark green crystals were produced again but of the composition $[Zn(L^1)_2]$ (**2**). This material is diamagnetic. Its ^{1}H NMR spectrum is identical to that reported by Girgis and Balch,[2] as is the orthorhombic space group $C222_1$ reported for this species by Pierpont et al.[7] The UV−vis spectrum of **2** in CH_2Cl_2 solution is also identical to that reported by Girgis and Balch with respect to the number and positions (λ_{max}) of observed transitions, but the observed molar extinction coefficients are ∼$^1/_5$ of those given by Girgis and Balch.[2] We cannot offer an explanation for this discrepancy.

When we carefully checked the microcrystals of different preparations of **2** under a microscope, we discovered that from time to time a few red crystals of a different habit had precipitated along with the large majority of dark green crystals of **2**. Since the red crystals were of X-ray quality, we selected a suitable specimen, mounted it on a Siemens SMART X-ray diffractometer, and determined its crystal structure (see below). The result confirmed its composition as $[Zn(C_{28}H_{40}NO_2)_2]$ (as in **2**), but it crystallized in a different space group (triclinic $P\bar{1}$), and the overall structure showed small but significant differences in comparison with the structure of **2** (see below). Having

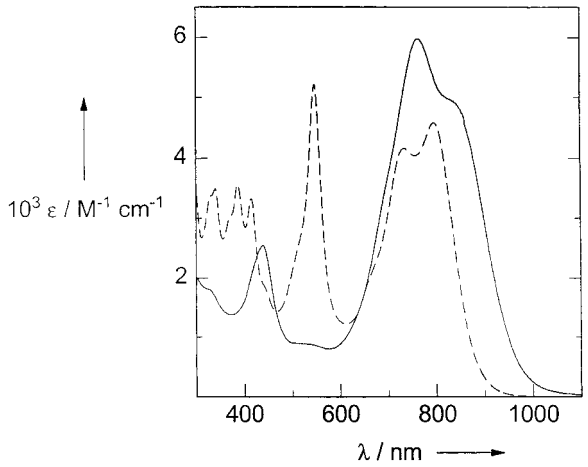

Figure 2. Electronic spectra of **2** (—) and **3** (- - -) in THF at 20 °C.

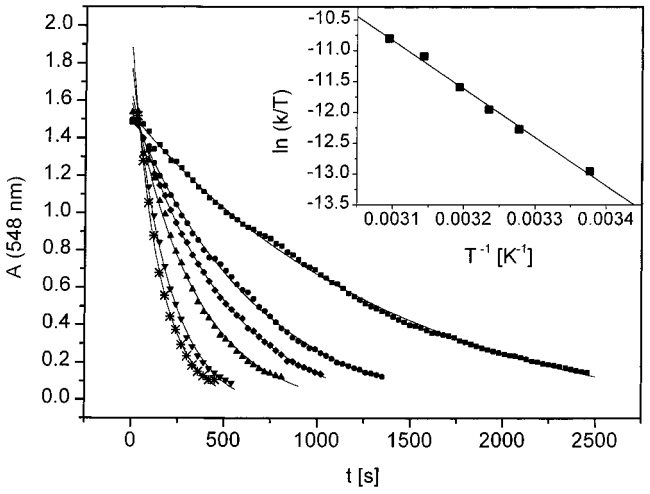

Figure 3. Plot of the absorbance at 548 nm of **3** in THF as a function of the time and temperature: *, 23; ▼, 32; ▲, 36; ◆, 40; ●, 45; ■, 50 °C. The inset shows the corresponding Eyring plot.

convinced ourselves that the green and red forms of $[Zn(C_{28}H_{40}NO_2)_2]$ are isomers, we searched for a synthetic route that would produce the red form in a reproducible manner and better yield.

This was achieved using the following protocol. The reaction of $[H_4L^3](CF_3CO_2)$ and $Zn(BF_4)_2 \cdot 2H_2O$ was performed in a 1:1 ratio (!) under anaerobic conditions in dry acetonitrile. A small amount of the auxiliary base NEt_3 had been added, and the reaction proceeded forward upon heating to reflux a pale yellow solution. Upon exposure of this solution to air at 20 °C, a color change to green occurred within 2 min. Addition of *n*-pentane initiated the precipitation of green microcrystals of **2** in ~70% yield. After filtration, the resulting solution is red-violet. Upon addition of $[(n\text{-}Bu)_4N](ClO_4)$ (salt effect), red crystals of the red form **3** precipitated within 12 h in ~25% yield (based on starting material $[H_4L^3](CF_3CO_2)$).

Temperature-dependent magnetic susceptibility measurements on a solid sample of pure red crystals of **3** on a SQUID magnetometer revealed a temperature-independent magnetic moment of 2.43 μ_B/molecule in the range 70−290 K, which then decreases monotonically to 2.27(1) μ_B at 5 K (see Figure 1). This indicates the presence of two essentially uncoupled unpaired electrons per molecule ($\mu_{eff} = (\mu_1^2 + \mu_2^2)^{1/2}$ with $\mu_1 = \mu_2 = 1.73\ \mu_B$, $\mu_{eff} = 2.45\ \mu_B$). The temperature dependence can be fitted using the Hamiltonian $H = -2JS_1S_2$ where $S_1 = S_2 = {}^1/_2$ with $g_1 = g_2 = 2.007$ and $J = -1.0$ cm^{-1}. This is shown in Figure 1. It is noted that the fit is not very sensitive to the actual value of *J*. The fit is quite reasonable in the limit from $J = 0$ to -1.0 cm^{-1}. Thus, the bulk susceptibility measurements do not allow to unambiguously identify a very small antiferromagnetic exchange coupling of the order of ~1.0 cm^{-1}, which is inter- rather than intramolecular as is shown by EPR spectroscopy (see below).

Given the composition and neutral charge of the red form **3** and its paramagnetic nature (two unpaired electrons per molecule), a charge distribution as $[Zn(L^2)(L^0)]$ appears to be the only reasonable interpretation of the data. Thus, the diamagnetic green form **2** and its red paramagnetic form **3** differ only by their respective charge distribution in the two coordinated ligands, which renders the two forms of ligand-based redox isomers.

Interestingly, when red crystals of **3** are dissolved in methanol at 20 °C under anaerobic conditions, the resulting solution is green and the ^1H NMR spectrum of diamagnetic **2** can be recorded. Thus, in polar solvents, the red form isomerizes rapidly to the green form, eq 1.

$$\underset{\text{red, paramagnetic}}{[Zn^{II}(L^2)(L^0)]} \rightarrow \underset{\text{green, diamagnetic}}{[Zn^{II}(L^1)_2]} \quad (1)$$

The reaction in eq 1 can be formally regarded as ligand-based comproportionation.

In contrast, red crystals of **3** dissolved in dry tetrahydrofuran, *n*-pentane, $CHCl_3$, or CH_2Cl_2 give red, paramagnetic solutions. In the absence of moisture, such solutions of **3** are fairly stable for a few minutes at 20 °C. On the other hand, THF solutions of green **2** are green and diamagnetic; **3** does not form in measurable amounts. In fact, we have not found conditions where green **2** is converted to red **3** in solution. Obviously, **2** is the thermodynamically more stable form.

Figure 2 shows the UV−vis spectra of **2** and **3** in THF at 20 °C. Clearly, the two species display significantly different electronic spectra. The spectra of **2** dissolved in CH_2Cl_2 and THF show a marked solvatochromism. The differences are not due to varying amounts of **3** present in the two solvents because **3** displays a very intense absorption maximum at 548 nm that is absent in the spectra of both solutions.

We have spectrophotometrically measured the kinetics of the conversion of **3** to **2** in THF as a function of the temperature (Figure 3). The process follows first-order kinetics (eq 2), indicating that the isomerization reaction is an intramolecular process.

$$d[\mathbf{2}]/dt = k[3] \quad (2)$$

First-order rate constants at 23, 32, 36, 40, 45, and 50 °C are $0.70(1) \times 10^{-3}$, $1.43(3) \times 10^{-3}$, $1.99(3) \times 10^{-3}$, $2.89(12) \times 10^{-3}$, $4.8(2) \times 10^{-3}$, and $6.5(2) \times 10^{-3}$ s^{-1}, respectively. The activation parameters (Eyring) are $\Delta H^{\ddagger} = 15.6 \pm 0.6$ kcal mol^{-1} and $\Delta S^{\ddagger} = -20.4 \pm 1.8$ cal mol^{-1} K^{-1}. They closely resemble data reported for the racemization of $[Cr(phen)_3]^{3+}$.[12] The large negative entropy of activation indicates that in order to overcome a substantial Franck−Condon barrier for a one-electron transfer from the L^2 ligand to L^0 with formation of two L^1 ligands, a highly ordered transition state of the two ligands L^2 and L^0 in **3** must be achieved. This could involve a twist mechanism,[12] as in the above example of $[Cr(phen)_3]^{3+}$.

The infrared spectra of **2** and **3** were recorded as KBr disks where care was taken to avoid pressurizing the sample above 1 atm during the preparation of the disks. Above 1 atm of pressure,

(12) Lawrance, G. A.; Stranks, D. R. *Inorg. Chem.* **1977**, *16*, 929.

Table 3. Electrochemistry of Complexes

complex	$E_{1/2}$, V vs Fc^+/Fc				ref
1	−0.29		−1.28		this work
$[Cu^{II}(L^2)(NEt_3)]$	−0.14		−1.06		10
2	+0.83	+0.43	−1.06	−1.28	this work
2[b]	0.68	0.34	−1.17	−1.50	4
2 (THF)	+0.71	+0.35	−1.05	−1.47	this work
$[Ni(L^1)_2]$[b]	+0.70	+0.33	−1.20	−1.53	4
3[c]	+0.90, +0.72, +0.37, +0.17		−0.91, −1.13, −1.34, −1.46		this work

[a] Conditions: CH_2Cl_2 solutions containing 0.10 M $[N(n\text{-butyl})_4]PF_6$ ($[TBA]PF_6$) supporting electrolyte; glassy carbon working electrode; $E_{1/2}$ values recorded at scan rates 100 mV/s and are referenced to the ferrocenium/ferrocene (Fc^+/Fc) couple. [b] Solvent in the original paper not specified. [c] Measured in THF at scan rate 100 mV/s.

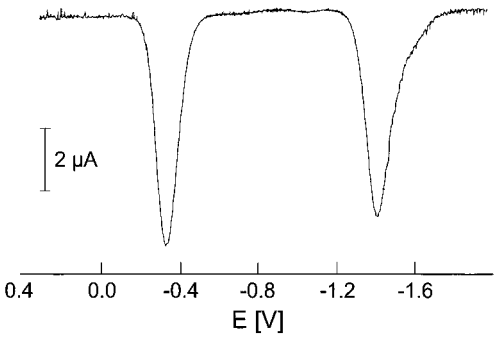

Figure 4. Square-wave voltammogram of **1** in CH_2Cl_2 (0.1 M $[TBA]PF_6$; glassy carbon working electrode; frequency 20 Hz; pulse height 25 mV).

the isomerization **3** → **2** is fast. The two spectra display some interesting differences in the range 1700−800 cm^{-1}. A single strong band at 1297 cm^{-1} in the spectrum of **2** is assigned to a ν(C−O) stretching frequency of predominantly phenolate character; in the spectrum of **3**, this band is split into two bands at 1308 and 1294 cm^{-1}, indicating an increase in the C−O bond strength and a decrease that we associate with the differing oxidation levels of L^0 (more C═O double bond character) and L^2 with less C═O double bond character than is observed for L^1 in **2**. Similarly, in the region 1470−1670 cm^{-1}, complex **2** displays a single strong band at 1528 cm^{-1} that is absent in the spectrum of **3** but where two new modes at 1635 and 1509 cm^{-1} are observed (ν(C−N) modes). Thus, the infrared spectra corroborate the notion that green $[Zn(L^1)_2]$ contains a single ligand type, and red $[Zn(L^0)(L^2)]$ contains two different ligands. Interestingly, with increasing oxidation level of L^n going from L^2 to L^1 to L^0 the ν(C═N) frequency increases from 1508 to 1528 to 1635 cm^{-1}, and, similarly, for the ν(C−O) stretch the trend is 1294 to 1297 to 1308 cm^{-1}.

Electro- and Spectroelectrochemistry. Cyclic and square-wave voltammograms of complexes **1**, **2**, and **3** were recorded in CH_2Cl_2 or THF solutions containing 0.10 M $[TBA]PF_6$ as the supporting electrolyte at a glassy carbon working electrode. Ferrocene was used as an internal standard, and all potentials were referenced versus the ferrocenium/ferrocene couple (Fc^+/Fc). The results are summarized in Table 3.

Figure 4 displays the square-wave voltammogram of **1** in CH_2Cl_2. Clearly, two reversible one-electron-transfer waves are observed, one of which corresponds to a reversible one-electron oxidation of **1** and the other one to a reduction, eq 3,

$$[Zn^{II}(L^1)(NEt_3)]^+ \underset{-e}{\overset{+e}{\rightleftharpoons}} \mathbf{1} \underset{-e}{\overset{+e}{\rightleftharpoons}} [Zn^{II}(L^3)(NEt_3)]^- \qquad (3)$$

as was established by coulometry at appropriately fixed potentials.

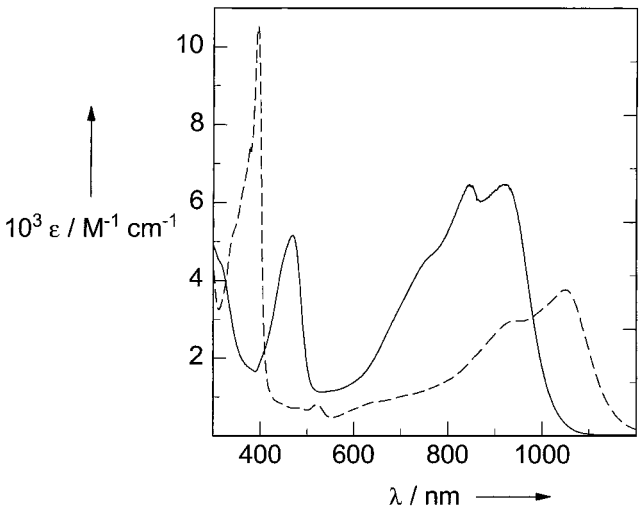

Figure 5. UV−vis spectra of the electrochemically one-electron oxidized (—) and reduced (- - -) form of **1** in CH_2Cl_2.

Both the oxidized and reduced forms are stable on the time scale of these experiments (∼10 min), as was established by subsequently recorded CVs of these forms that were identical to that of **1**. UV−vis absorption spectra of the oxidized and reduced forms have been recorded and are shown in Figure 5. This series of complexes allows one to obtain the electronic spectra of the coordinated pure ligands $(L^1)^{1-}$, $(L^2)^{2-}$, and $(L^3)^{3-}$ (see also Table 4). The CH_2Cl_2 solution containing $[Zn(L^1)(NEt_3)]^+$ is violet, that of **1** is green, and that of $[Zn(L^3)(NEt_3)]^-$ is pale green-yellow. Note that all redox processes are ligand-centered. Thus, in the potential range +0.3 to −1.6 V vs Fc^+/Fc, three ligand-based oxidation levels are accessible for complex **1**.

Figure 6 shows the corresponding CV and square-wave voltammograms of green **2** in CH_2Cl_2. Two reversible one-electron oxidation and two one-electron reduction waves are now observed in excellent agreement with the measurements reported previously by Pierpont et al.[4] We assign these processes as in eq 4.

$$[Zn(L^0)_2]^{2+} \underset{-e}{\overset{+e}{\rightleftharpoons}}{}^{E^1_{1/2}} [Zn(L^0)(L^1)]^+ \underset{-e}{\overset{+e}{\rightleftharpoons}}{}^{E^2_{1/2}} \mathbf{2} \underset{-e}{\overset{+e}{\rightleftharpoons}}{}^{E^3_{1/2}} [Zn(L^1)(L^2)]^- \underset{-e}{\overset{+e}{\rightleftharpoons}}{}^{E^4_{1/2}} [Zn(L^2)_2]^{2-} \qquad (4)$$

Coulometric measurements in combination with subsequent cyclic voltammetry established that the monocation, the neutral species **2**, and its one- and two-electron reduced species are stable on the time scale of these experiments but not the dication which decomposes. In the potential range +1.0 to −1.6 V vs Fc^+/Fc, the three ligand oxidation levels L^0, $(L^1)^{1-}$, and $(L^2)^{2-}$ are now accessible but *not* $(L^3)^{3-}$. The electronic spectra of electrochemically generated deep red $[Zn(L^0)(L^1)]^+$ and of neutral green **2** are shown in Figure 7 (top), whereas those of the reduced forms green $[Zn(L^1)(L^2)]^-$ and light green $[Zn(L^2)_2]^{2-}$ are displayed in Figure 7 (bottom).

Note that the spectra of **1** and $[Zn(L^2)_2]^{2-}$ are quite similar, but the latter is not simply the spectrum of **1** with twice the intensity, which is what one might have anticipated considering that **1** contains the chromophore $(L^2)^{2-}$ and $[Zn(L^2)_2]^{2-}$ has two of these. Also, the spectra of **2** and $[Zn(L^1)(NEt_3)]^+$ are similar since both contain only $(L^1)^{1-}$ ligands.

Table 4. Electronic Spectra

complex	solvent	λ_{max}, nm (ϵ, L mol^{-1} cm^{-1})
1	THF	391 (6.1 × 10^3), 436 (3.8 × 10^3), 510 sh, 769 (4.9 × 10^3), 867 (4.6 × 10^3), 1011 (1.4 × 10^3)
	CH_2Cl_2	362 (6.7 × 10^3), 394 (7.3 × 10^3), 444 (1.4 × 10^3), 529 (933), 902 (3.4 × 10^3), 1060 (2.3 × 10^3)
[**1**]$^{+}$ [a]	CH_2Cl_2 [b]	470 (5.1 × 10^3), 780 sh, 850 (6.0 × 10^3), 922 (6.4 × 10^3)
[**1**]$^{-}$ [a]	CH_2Cl_2 [b]	350 sh, 395 (1.0 × 10^4), 522 (800), 948 (2.9 × 10^3), 1050 (3.7 × 10^3)
2	CH_2Cl_2	370 (2.1 × 10^3), 431 (2.5 × 10^3), 732 (9.4 × 10^3), 794 (8.2 × 10^3)
	THF	330 (1.8 × 10^3), 440 (2.4 × 10^3), 764 (5.9 × 10^3), 840 (5.0 × 10^3)
[**2**]$^{+}$ [a]	CH_2Cl_2 [b]	377 (1.6 × 10^3), 433 (2.4 × 10^3), 547 (2.3 × 10^3), 735 (5.8 × 10^3), 789 (5.1 × 10^3)
[**2**]$^{-}$ [a]	CH_2Cl_2 [b]	368 (2.3 × 10^3), 415 (3.2 × 10^3), 733 (9.0 × 10^3), 787 (8.1 × 10^3), 968 (840)
[**2**]$^{2-}$ [a]	CH_2Cl_2 [b]	413 (4.7 × 10^3), 751 (5.7 × 10^3), 787 (5.8 × 10^3), 975 (1.8 × 10^3)
3	THF	338 (3.4 × 10^3), 385 (3.6 × 10^3), 413 (3.3 × 10^3), 548 (5.2 × 10^3), 733 (4.2 × 10^3), 795 (4.6 × 10^3)

[a] Electrochemically generated by controlled potential electrolysis (coulometry). [b] Supporting electrolyte 0.10 M $[N(n\text{-but})_4]PF_6$.

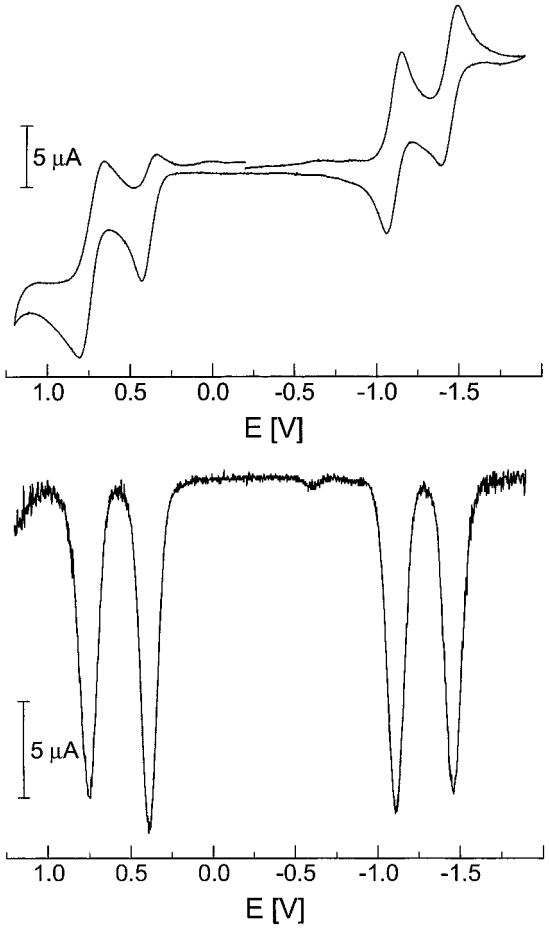

Figure 6. Cyclic and square-wave voltammograms of **2** in CH_2Cl_2 (0.10 M $[TBA]PF_6$). Potentials are referenced in volts vs Fc^+/Fc. Conditions: CV, glassy carbon electrode, scan rate 100 mV s^{-1}; square-wave, pulse height 25 mV, frequency 20 Hz.

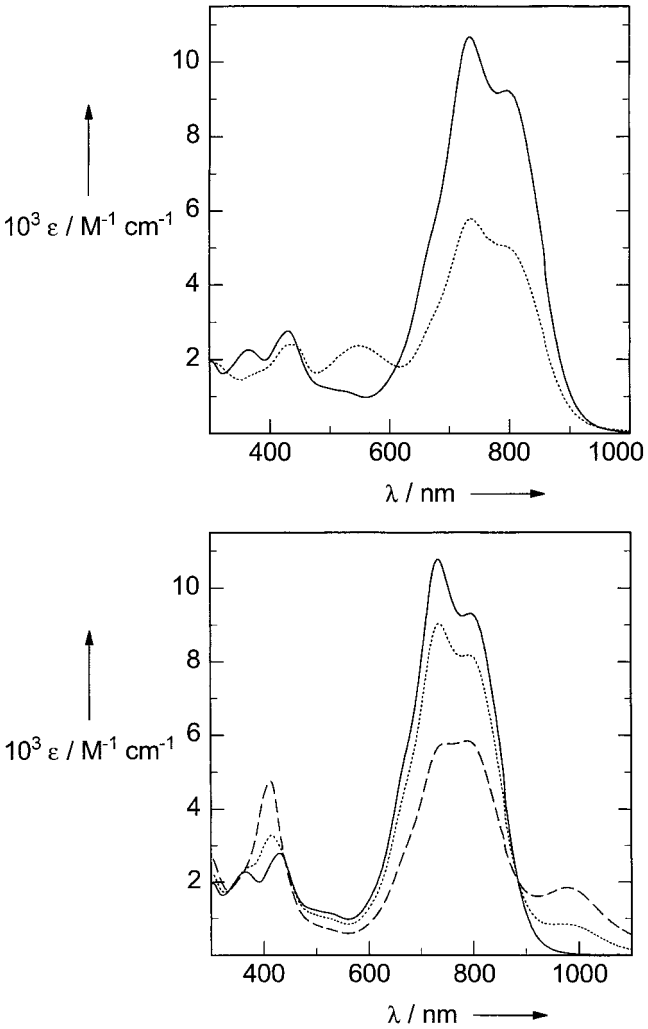

Figure 7. (top) Electronic spectra of **2** (—) and its one-electron oxidized form $[Zn(L^0)(L^1)]^+$ (•••) in CH_2Cl_2 (0.10 M $[TBA]PF_6$). (bottom) Spectra of electrochemically generated reduced forms $[Zn(L^1)(L^2)]^-$ (•••) and $[Zn(L^2)_2]^{2-}$ in CH_2Cl_2 (0.10 M $[TBA]PF_6$).

Finally, we have recorded a square-wave voltammogram of a red THF solution of **3** (0.10 M $[TBA]PF_6$) immediately after the crystals of **3** had dissolved. This is shown in Figure 8 (top). Interestingly, eight one-electron transfer processes are observed during the very first sweep. The second sweep, shown in Figure 8 (middle), was immediately recorded after completion of the first, and the third (Figure 8 (bottom)) was recorded after a ~5 min delay. Clearly, four of the primary eight one-electron transfer processes disappear with time upon repetitive sweeping, namely, those at $E_{1/2}$ values of +0.91, +0.15, −0.91, and −1.33 V. The remaining four processes are identical to those observed for a green THF solution of **2**, which do not change as a function of time or number sweeps. This behavior implies that there are two different species in solution, one of which being rapidly isomerized to the other upon one-electron oxidation (or reduction). Note that the simple thermal isomerization of red **3** to green **2** in THF is comparatively slow on the time scale of the above electrochemical experiments ($t_{1/2}$ ~10 min). We have not attempted to further analyze the dynamics of these processes, but it is obvious that red **3** displays the same number of redox active steps (four) but at different potentials as the thermodynamically more stable **2**. We tentatively assigned the four redox steps for **3** as shown in eq 5.

$$[Zn(L^0)_2]^{2+} \underset{-e}{\overset{+e}{\rightleftharpoons}} [Zn(L^0)(L^1)]^{+} \underset{-e}{\overset{+e}{\rightleftharpoons}} [Zn(L^0)(L^2)] \ (\mathbf{3}) \underset{-e}{\overset{+e}{\rightleftharpoons}} [Zn(L^1)(L^2)]^{-} \underset{-e}{\overset{+e}{\rightleftharpoons}} [Zn(L^2)_2]^{2-} \quad (5)$$

$$E'^{1}_{1/2} \qquad E'^{2}_{1/2} \qquad E'^{3}_{1/2} \qquad E'^{4}_{1/2}$$

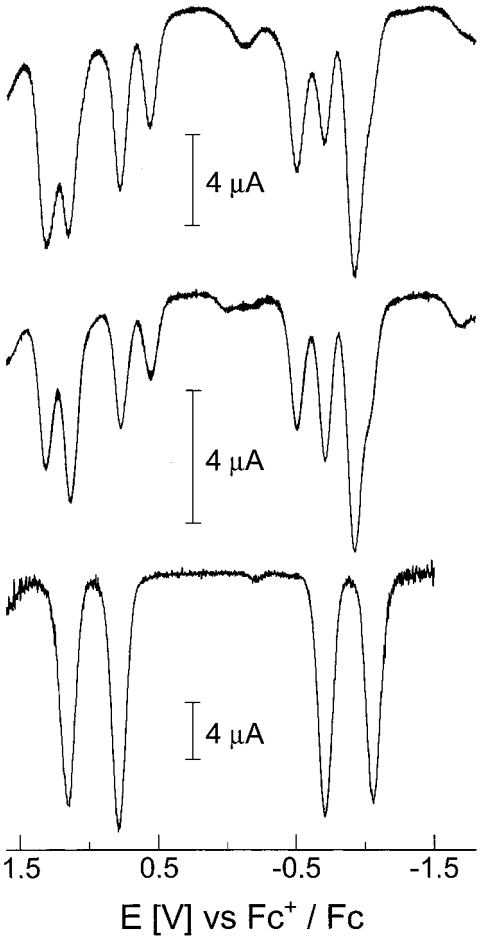

Figure 8. Square-wave voltammograms of **3** in THF recorded (a) within 2 min after the crystals had dissolved (top), (b) a second sweep measured directly after the first (middle), and (c) a third after a 5 min delay. Conditions: top, pulse height 25 mV, frequency 60 Hz; middle, 25 mV, 20 Hz; bottom, 25 mV, 20 Hz.

It appears to be plausible that the potentials $E'^2_{1/2}$ and $E'^3_{1/2}$ in eq 5 are different from $E^2_{1/2}$ and $E^3_{1/2}$, respectively, in eq 4 because both involve oxidation and reduction of a ligand in a different oxidation level, i.e., $(L^1)^-$ to L^0 in **2** and $(L^2)^{2-}$ to $(L^1)^-$ in **3**, on the one hand, and $(L^1)^-$ to $(L^2)^{2-}$ in **2** and (L^0) to $(L^1)^-$ in **3** on the other hand. In contrast, following the same line of arguments, one might expect that $E'^1_{1/2} = E^1_{1/2}$ and $E'^4_{1/2} = E^4_{1/2}$ because the redox couples involve the same redox levels of the ligand; i.e., the couples $[Zn(L^0)_2]^{2+}/[Zn(L^0)(L^1)]^+$ and $[Zn(L^1)(L^2)]^-/[Zn(L^2)_2]^{2-}$. This is obviously not the case, although it is noted that the differences $|E'^2_{1/2} - E^2_{1/2}|$ and $|E'^3_{1/2} - E^3_{1/2}|$ of 200 and 220 mV, respectively, are somewhat larger than those between $|E'^1_{1/2} - E^1_{1/2}|$ of 180 mV and $|E'^4_{1/2} - E^4_{1/2}|$ of 120 mV. We take these results as an indication that the differing conformation of the ligands in **2** and **3** is retained upon successive oxidation and reduction albeit for a short period of time (on the time scale of one cyclic voltammetry experiment).

Crystal Structures. Crystals of **1** consist of neutral molecules $[Zn^{II}(L^2)(NEt_3)]$, the molecular structure of which is shown in Figure 9. Selected bond distances and angles are given in Table 5. The central zinc ion is four-coordinate. The paramagnetic tridentate ligand $(L^2)^{2-}$ and a monodentate neutral triethylamine ligand give rise to a nearly square planar N_2O_2Zn coordination polyhedron. Complex **1** is isomorphous and isostructural with its copper(II) analogue $[Cu^{II}(L^2)(NEt_3)]$.[10] The dihedral angle between the two "aromatic" rings of the coordinated $(L^2)^{2-}$ ligand is 20.1°; the tridentate ligand L^2 is not coplanar.

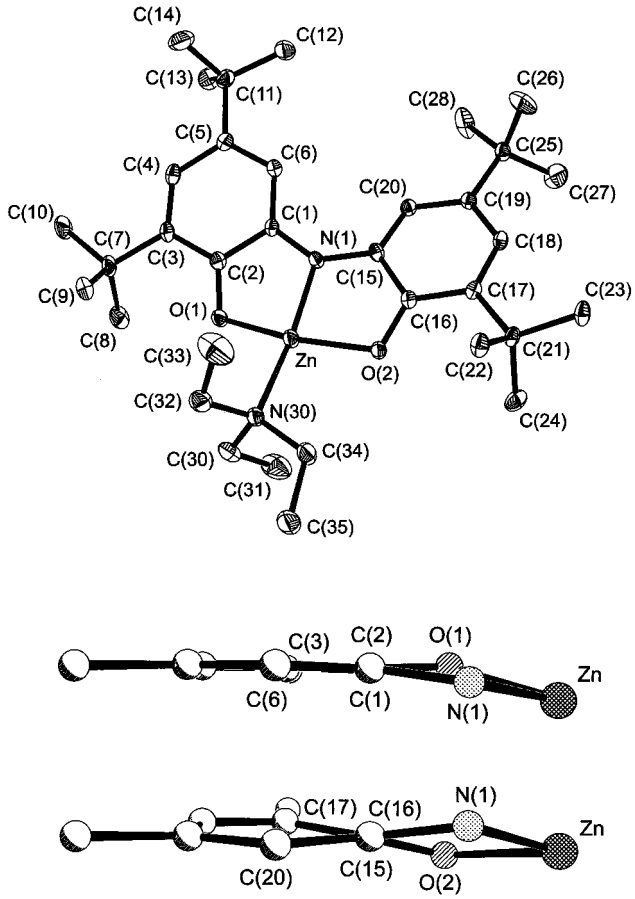

Figure 9. Perspective view of the neutral molecule in crystals of **1** (the thermal ellipsoids are drawn at the 40% level) and Newman projections looking down the C1−C2 and C15−C16 bonds emphasizing the differing conformations of the six-membered carbon rings of coordinated L^2.

It is noted that the two Zn−O, the two C−N, and the two C−O distances are different within the 3σ limit, respectively. This points to a slightly asymmetric localized distribution of the electron density within the $(L^2)^{2-}$ ligand as depicted by two resonance structures **A** and **B**. This is corroborated by the

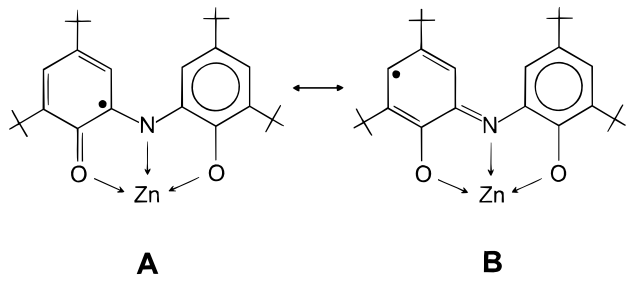

A **B**

observation that the longer Zn−O2 distance at 1.955(2)° is followed by the *shorter* O−C distance (O2−C16 at 1.309(3) Å) and then by the *shorter* C−N bond (N1−C15 at 1.352(3) vs N1−C1 at 1.381(3) Å), both of which are attached to the same C15−C20 ring. This ring displays more iminosemiquinone character than the other one that is more aromatic. This is also substantiated by the fact that the sums of the six C−C distances of the two rings of coordinated $(L^2)^{2-}$ differ by 0.027 Å, where the iminosemiquinone ring (C15−C20) is slightly larger than the more aromatic ring (C1−C6). Furthermore, the two dihedral angles O1−C2···C1−N1 and O2−C16···C15−N1 are different at 10.4° and 18.6°, respectively, and the mean deviation of the

Table 5. Selected Bond Distances (Å) and Angles (°) in **1**, **2**, and **3**

	1	**2** (green)	**3** (red)
Zn−O1	1.926(2)	2.154(2)	2.049(2)
Zn−O2	1.955(2)	2.119(2)	2.052(2)
Zn−N1	1.907(2)	2.086(2)	2.139(2)
Zn−O3		2.140(2)	2.075(2)
Zn−O4		2.155(2)	2.073(2)
Zn−N2		2.074(2)	2.124(2)
Zn−N30	2.011(2)		
O1−C2	1.318(3)	1.260(3)	1.265(3)
C1−C2	1.433(3)	1.476(4)	1.475(4)
C2−C3	1.423(3)	1.453(4)	1.453(4)
C3−C4	1.385(4)	1.365(4)	1.364(4)
C4−C5	1.411(4)	1.438(4)	1.437(4)
C5−C6	1.380(4)	1.354(4)	1.359(4)
C6−C1	1.413(3)	1.425(4)	1.429(4)
N1−C1	1.381(3)	1.328(3)	1.342(4)
O2−C16	1.309(3)	1.272(3)	1.264(3)
C15−C16	1.438(4)	1.462(4)	1.472(4)
C16−C17	1.434(3)	1.459(4)	1.457(4)
C17−C18	1.387(4)	1.367(4)	1.360(4)
C18−C19	1.422(3)	1.421(4)	1.440(4)
C19−C20	1.373(4)	1.367(4)	1.360(4)
C20−C15	1.418(4)	1.419(4)	1.427(4)
N1−C15	1.352(3)	1.346(3)	1.342(4)
O3−C30		1.265(3)	1.259(3)
C29−C30		1.467(4)	1.469(4)
C30−C31		1.458(4)	1.453(4)
C31−C32		1.359(4)	1.361(4)
C32−C33		1.436(4)	1.436(4)
C33−C34		1.364(4)	1.358(4)
C34−C29		1.422(4)	1.422(4)
N2−C29		1.346(4)	1.339(4)
O4−C44		1.272(4)	1.270(3)
C43−C44		1.467(4)	1.468(4)
C44−C45		1.457(4)	1.457(4)
C45−C46		1.361(4)	1.363(4)
C46−C47		1.440(4)	1.426(4)
C47−C48		1.353(4)	1.356(4)
C48−C43		1.419(4)	1.431(4)
N2−C43		1.340(4)	1.341(4)
N2−Zn−N1		176.07(9)	175.27(9)
N2−Zn−O2		106.63(8)	102.41(9)
N1−Zn−O2	83.34(8)	77.22(8)	77.95(9)
N2−Zn−O3		76.81(8)	77.48(9)
N1−Zn−O3		102.11(8)	97.81(9)
O2−Zn−O3		97.37(8)	92.51(8)
N2−Zn−O1		99.80(8)	101.58(8)
N1−Zn−O1	83.79(8)	76.34(8)	78.25(9)
O2−Zn−O1	159.93(8)	153.57(8)	155.97(8)
O3−Zn−O1		88.26(8)	93.92(8)
N1−Zn−O4		104.60(8)	106.69(9)
O2−Zn−O4		88.93(8)	93.29(8)
O3−Zn−O4		153.29(8)	155.49(8)
O1−Zn−O4		97.58(8)	90.39(8)
N1−Zn−N30			
O1−Zn−N30			
O2−Zn−N30			

six carbon atoms from its best plane is 0.002 Å for the C1⋯C6 ring but 0.044 Å for the C15−C20 ring. Again, these data point to a more aromatic C1−C6 phenyl ring (planar), whereas the other C15−C20 ring (nonplanar) has iminosemiquinone character. Interestingly, Tuck et al.[8a] have reported the crystal structure of green, diamagnetic $[Pb(L^1)_2]$ where the coordinated diamagnetic ligands $(L^1)^-$ have also an asymmetric electron density distribution as is represented by structure **C**. One aromatic ring and an iminobenzoquinone ring per L^1 are structurally discernible. This is in stark contrast to the structures of $[Ni(L^1)_2]$ and **2**, both of which contain $(L^1)^-$ ligands with a *symmetric* electron density.

Crystals of both **2** and **3** consist of neutral molecules $[Zn(C_{28}H_{40}NO_2)_2]$ where the six-coordinate zinc ions bind meridionally two tridentate ligands L^n. Figure 10 shows the structure of such a molecule in red **3**; that of the corresponding molecule in **2** is not shown as it is very similar. We use the same atom labels for both structures. Compound **2** crystallizes in the chiral orthorhombic space group $C222_1$, whereas **3** crystallizes in the centrosymmetric triclinic space group $P\bar{1}$. Thus, all molecules in **2** have $M(\Lambda\Lambda)$ configuration (or in a different crystal $M(\Delta\Delta)$), whereas in crystals of **3** both enantiomers are present in equal amounts. For the following discussion, it is important to note that the neutral molecules in both **2** and **3** do not possess crystallographically imposed symmetry.

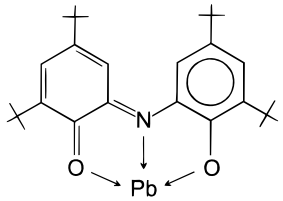

C

Figure 11 displays the core structures of the neutral species in **2** and **3** where the tertiary butyl groups are not shown for the sake of clarity. Both molecules are oriented in such a way that the N−Zn−N vector runs perpendicularly above and below the paper plane, while the Zn ion resides in this plane. This representation emphasizes the fact that the dihedral angles θ between the two "aromatic" C_6 planes of a given ligand L^n are very different in both structures: in **2** these two angles are 29.2 and 31.3°, whereas in **3** they are 8.9 and 13.6°. Inspection of the data in Table 1 immediately reveals that this angle does not correlate with the oxidation level of $(L^n)^{n-}$. As other workers have pointed out, it probably is primarily determined by packing effects. The data in Table 1 show that all complexes crystallizing in the orthorhombic space group $C222_1$ have large twist angles ($>25°$) whereas those crystallizing in the triclinic space group $P\bar{1}$ have small θ values ($<15°$), irrespective of the oxidation level of L^n. However, the smaller the θ values, the more delocalization of the unpaired spin in the paramagnetic ligands L^2 and L^0 over both ring systems can be expected (symmetric electron density distribution). Thus, the slight structural differences between the two rings of L^2 observed in **1** where θ is 20.1° are barely observed in **3** where the metrical details of the ring systems of L^2 (and L^0) are very similar. As noted above, the electron density distribution of L^1 in **2** is symmetric; both rings exhibit the same metrical details.

In the following, we compare the two ZnN_2O_4 polyhedra in **2** and **3**. In **2**, the four Zn−O and two Zn−N bonds are within experimental error, respectively, and the average Zn−O distance at 2.14 ± 0.01 Å is significantly longer than the average Zn−N distance at 2.08 ± 0.01 Å. This sequence has also been observed in **1**, which contains an $(L^2)^{2-}$ ligand. In contrast, in **3**, the two Zn−O bonds of one ligand at an average 2.05 ± 0.01 Å are slightly (but significantly) shorter than the corresponding two bonds of the second ligand at 2.074 ± 0.01 Å; the two Zn−N distances are different and, in both cases, *longer* than the corresponding Zn−O bond distances. These data clearly show that **2** contains two identical ligands, whereas in **3**, there are two slightly different ones. It appears to be plausible to associate the two longer Zn−O bonds in **3** with a more highly oxidized (less negatively charged) neutral ligand L^0 and the other one with the dianionic ligand $(L^2)^{2-}$. One would then simplistically expect the Zn−O bonds in **2** to be intermediate between those of L^2 and L^0 in **3** but this is not observed.

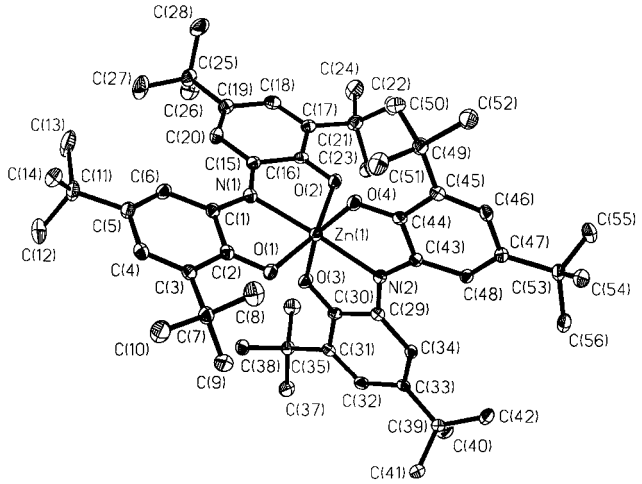

Figure 10. Perspective view of a neutral $[Zn(L^2)(L^0)]$ molecule in crystals of **3**.

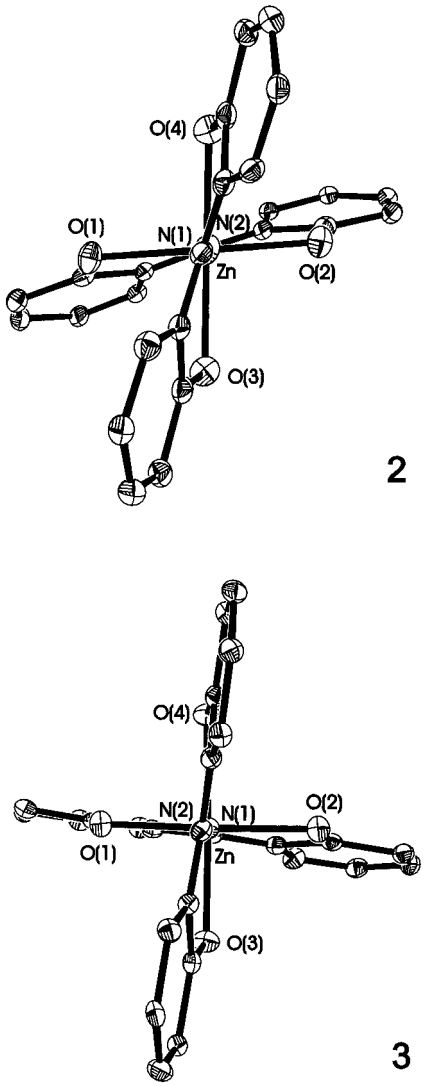

Figure 11. Core structures of the neutral molecules in **2** and **3**. (The N−Zn−N axis is oriented perpendicular to the paper plane where the Zn ions lie in this plane.)

There are no obvious strong intermolecular contacts between the neutral molecules in crystals of **2** or **3** that might induce (or stabilize) the charge separation in **3**. Thus, solid-state effects do not appear to be the cause of the existence of the metastable redox isomer **3**. This is of course also substantiated by the fact

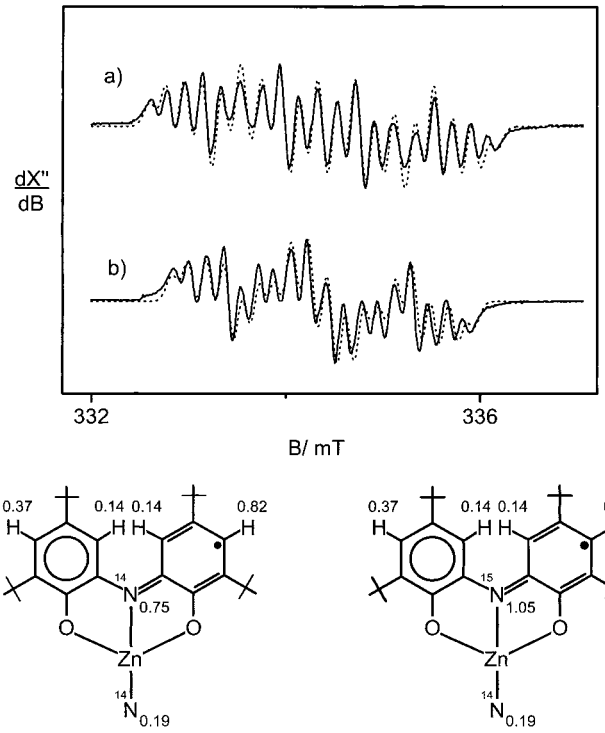

Figure 12. Experimental (—) and simulated (···) X-band EPR spectra of **1** in CH_2Cl_2 (7.5×10^{-4} M) at 298 K (microwave power, 10 mW; modulation amplitude, 0.05 mT; gain, 500). The hyperfine coupling constants are given in mT. Spectrum (a) ^{14}N in natural abundance in **1**; (b) ^{15}N-labeled L^2 in **1**.

that molecules of **3** have a measurable lifetime in solution. A related observation has been reported for the valence tautomers $[Co^{II}(Opy2)(DBSQ)_2]/[Co^{III}(Opy2)(DBSQ)(DB\ Cat)]$ but, in this situation, solid-state effects stabilize the metastable Co^{II} isomer.[8b]

^{1}H NMR and X-Band EPR Spectroscopy. The ^{1}H NMR spectrum of diamagnetic **2** has been reported by Girgis and Balch. In excellent agreement with that measurement, we have observed in a 500 MHz ^{1}H NMR of **2** in $CDCl_3$ at 22 °C the following signals: $\delta = 1.20$ (s, 18H, *tert*-butyl), 1.30 (s, 18H, *tert*-butyl), 7.32 (d, 2H), 7.16 (d, 2H). This indicates the presence of two equivalent diamagnetic ligands $(L^1)^-$ in **2** in solution.

In contrast, for **1** dissolved in $CDCl_3$ at 22 °C, we have observed a paramagnetically shifted spectrum, comprising the following signals in the diamagnetic region: $\delta = 1.52$ (s, 9H, $N-CH_2CH_3$), 2.00 (s, 24 H, $N-CH_2-CH_3$ and 2-*tert*-butyl groups). The paramagnetically shifted broad signal at 5.6 (s, 18H, 2-*tert*-butyl groups) is assigned to two *tert*-butyl groups of the semiquinone ring. In addition, three strongly paramagnetically shifted signals have been observed at $\delta = -121.2$ (b, 1H), −69.0 (b, 1H), +44.3 (b, 2H), which are assigned to the four protons bound to two C_6 rings. The chemical shifts of these signals can be correlated with the hyperfine coupling constants (hfc), a_H, of the EPR spectrum of **1** (see Figure 12). The signal at −121 ppm corresponds then to the proton at the iminosemiquinone ring in the para position relative to the imino nitrogen, whereas that at −69.0 ppm is assigned to the proton at the phenyl ring, again in para position to the nitrogen. The broad signal (2H) at +44.3 ppm must then be assigned to the two protons with similar small hfc's, both of which are in ortho positions relative to the nitrogen. This ^{1}H NMR spectrum clearly shows that the asymmetric electron density distribution in coordinated L^2 of **1** is retained in solution. It is not a consequence of the packing in the solid state.

The 500 MHz NMR spectrum of paramagnetic **3** in $CDCl_3$

(0.08 M) at 22 °C displays in the diamagnetic region four broad, barely resolved signals of eight *tert*-butyl groups at $\delta = 1.7$, 1.5, 1.33, and 1.30 and seven strongly paramagnetically shifted proton signals at −137, −123, −108, −70, −15, +17, and +44, which we assign to the ring protons of L^2 and L^0. A more detailed assignment is not possible, but the data do show that even in solution **3** contains two different paramagnetic ligands L^2 and L^0.

Figure 12 shows the X-band EPR spectra of **1** in CH_2Cl_2 solution at 298 K where the top spectrum was recorded using a sample of **1** that contained ^{14}N, ^{15}N in normal abundance, whereas the bottom spectrum was measured on a sample containing a selectively ^{15}N-labeled ligand $(L^2)^{2-}$. The spectra were successfully simulated (dotted lines) by using a set of hyperfine coupling constants (hfc) shown in Figure 12. Clearly, a strong coupling to the imino nitrogen ^{14}N or ^{15}N of L^2 ($a(^{15}N) = [\gamma(^{15}N)/\gamma(^{14}N)]a(^{14}N) = 1.40a(^{14}N)$) has been established and, in addition, a weaker coupling to the ^{14}N of the coordinated triethylamine. Furthermore, because of the asymmetric electron density distribution in the $Zn(L^2)$ moiety, there is a significantly different spin density at the two para positions with respect to the imino nitrogen ($a_H = 0.37$ and 0.82 mT). In contrast, the two protons in ortho positions relative to the imino nitrogen display the same hyperfine couplings ($a_H = 0.14$ mT). The g value of 2.003 ± 0.0005 is in excellent agreement with the value determined by the bulk magnetic susceptibility measurements (see above).

The X-band EPR spectrum of paramagnetic ($S_t = {}^1/_2$) [$Pb(L^2)(R)_2$] species has been reported,[13] and hyperfine coupling constants have been determined. Herein, a symmetric electron distribution has been invoked since the spectrum was successfully simulated with only two hydrogen hfc's at ~0.31 and 0.16 mT.

Figure 13 displays the X-band EPR spectrum of **3** in THF solution at 60 K.

The simulation was obtained by using a spin Hamiltonian for two coupled spins $S_1 = S_2 = {}^1/_2$, with an anisotropic coupling tensor $\mathbf{S_1 \cdot J \cdot S_2}$ in order to account for exchange and dipolar interactions.[14] The g values for both spins were fixed at 2.0055 (in close agreement with the magnetic susceptibility measurement) where possible differences between the g values of the two radicals L^2 and L^0 or anisotropies were not taken into account. The dipolar coupling (i.e., the traceless part of **J**) was

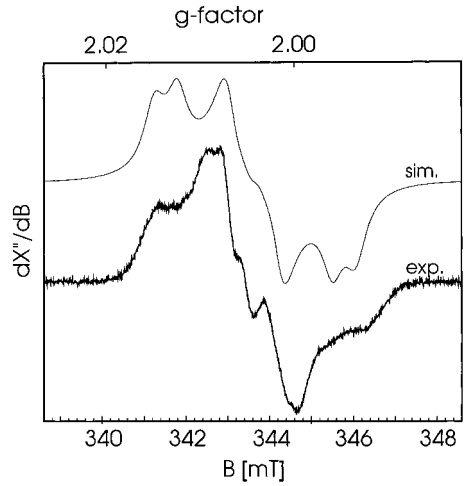

Figure 13. X-band EPR spectrum of **3** in THF at 60 K. Conditions: frequency, 9.6463 GHz; microwave power, 25 μW; modulation amplitude, 0.2 mT.

parametrized by $J_z = 0.006$ cm^{-1} and a "rhombic" distortion $|J_y - J_x| = 0.0032$ cm^{-1}. The quality of the simulation decreased significantly when isotropic contributions, $J_o = \mathrm{Tr}(\mathbf{J})/3 > 0.001$ cm^{-1}, from exchange interactions were included. Inclusion of larger exchange interactions yields a pronounced attenuation of the central peaks in the simulated spectrum, which is experimentally not observed. No other signals were detected in the field range 0−1 T. Hence, no other singlet−doublet transition occurs in this range, which gives rise to the additional constraint for exchange coupling of $J_o > 1.5$ cm^{-1} or $J_o < 0.01$ cm^{-1}. Thus, the spins in **3** are essentially uncoupled. We have not been able to obtain a better fit to the experimental spectrum because hyperfine interactions were not included in our Hamiltonian. However, the above analysis reproduces reliably the major features of the spin interaction of the uncoupled radical pair in **3**.

Acknowledgment. We thank Dipl.-Chem. R. Schumacher for the fit of the kinetic data. Financial support of this work from the Fonds der Chemischen Industrie is also gratefully acknowledged.

Supporting Information Available: Tables of crystallographic and structure refinement data, atom coordinates and U_{eq} values, bond lengths and angles, anisotropic thermal parameters, and calculated and refined positional parameters of hydrogen atoms for complexes **1**, **2**, and **3**. This material is available free of charge via the Internet at http://pubs.acs.org.

IC990003G

(13) Stegmann, H. B.; Scheffler, K.; Stöcker, F. *Angew. Chem.* **1970**, *82*, 481.

(14) Gaffney, B. J.; Silverstone, H. J. *Simulation of the EMR spectra of High-Spin Iron in Proteins*; Gaffney, B. J., Silverstone, H. J., Eds.; Plenum Press: New York, 1993; Vol. 13; the spin Hamiltonian was adapted and modified (Bill, E.; Mülheim).